Assessing the stability of Cd3As2 Dirac semimetal in humid environments: the influence of defects, steps and surface oxidation

Zhang Yanxue, Nappini Silvia, Sankar Raman, Bondino Federica, Gao Junfeng, Politano A.

Journal of Materials Chemistry C, Vol. 9 - 4, pp. 1235-1244 (2021)
doi: 10.1039/d0tc04883f (Journal Article)

Submitted
14 Oct 2020
Accepted
04 Dec 2020
First published
07 Dec 2020

Assessing the stability of Cd3As2 Dirac semimetal in humid environments: the influence of defects, steps and surface oxidation
Y. Zhang, S. Nappini, R. Sankar, F. Bondino, J. Gao and A. Politano, J. Mater. Chem. C, 2021, 9, 1235 DOI: 10.1039/D0TC04883F

Assessing the stability of Cd_3As_2 Dirac semimetal in humid environments: the influence of defects, steps and surface oxidation

Yanxue Zhang[1,§], Silvia Nappini[2,§], Raman Sankar[3], Federica Bondino[2,*], Junfeng Gao[1*], and Antonio Politano[4,5,*]

1 Key Laboratory of Materials Modification by Laser, Ion and Electron Beams (Dalian University of Technology), Ministry of Education, School of Physics, Dalian 116024, China

2 Consiglio Nazionale delle Ricerche (CNR)- Istituto Officina dei Materiali (IOM), Laboratorio TASC in Area Science Park S.S. 14 km 163.5 34149 Trieste, Italy
3 Center for Condensed Matter Sciences, National Taiwan University, Taipei 10617, Taiwan
4 Department of Physical and Chemical Sciences, University of L'Aquila, via Vetoio, 67100 L'Aquila (AQ), Italy
5 CNR-IMM Istituto per la Microelettronica e Microsistemi, VIII strada 5, I-95121 Catania, Italy

§ These authors contributed equally

The presence of a Dirac cone in bulk cadmium arsenide (Cd_3As_2) has triggered the interest of the scientific community, considering its technological potential related to the ultrahigh mobility of charge carriers and the observed giant magnetoresistance. Definitely, the stability of Cd_3As_2 in humid environments is crucial for a successful technology transfer. Here, we study the interaction of Cd_3As_2 with water by means of density functional theory and surface-science experimental tools. Metastable water adsorption is feasible for both pristine and defective surfaces with Cd and As vacancies. Water decomposition is energetically favorable only at steps, although with a rate of only ~0.1 s^{-1} at atmospheric pressure, with H and OH fragments forming bonds with As and Cd atoms, respectively. Interestingly, surface oxidization notably increases the reactivity towards water, also enabling water decomposition on the oxidized Cd_3As_2(112) surface with a rate of ~10^8 s^{-1} and an energy barrier of only 0.29 eV. Our study clarifies the key role of surface oxidation in the interaction of Cd_3As_2 with water molecules, and, consequently, also in the stability of Cd_3As_2 in humid environments (including air).Moreover, our results elucidate the need of encapsulation in order to protect the surface of Cd_3As_2 topological semimetal from oxidation and hydroxylation. Correspondingly, it is evident that the wetting properties of this topological material drastically depend on the presence of surface oxide phases.

*corresponding authors: Federica Bondino (bondino@iom.cnr.it); Junfeng Gao (gaojf@dlut.edu.cn) and Antonio Politano (antonio.politano@univaq.it)

1 Introduction

The observation of massless Dirac fermions in graphene has opened new avenues for science and technology[1-10]. As a matter of fact, Dirac-cone electrons provide a two-dimensional electron gas (2DEG) platform for next-generation electronic devices exploiting the ultrahigh mobility of charge carriers with quasi-relativistic velocity (c/300 in graphene, with c the light velocity) [11, 12]. Nevertheless, the isolation of monolayer graphene is complicated with exfoliation techniques with subsequent limitations for scale-up [13], while epitaxial growth implies in most cases hybridization of Dirac-cone states with substrate states [14-17]. Successively, Dirac fermions were observed also in other 2DEG systems, namely mono-elemental monolayer crystals (Xenes), such as silicene[18, 19], germanene[20] and borophene[21, 22]. Xenes do not exist in nature, while they can be stabilized with a supporting substrate for growth, nanofabrication and technological implementation [23]. Nevertheless, besides the intrinsic complication related to the obtainment of the single-layer regime, Dirac cone in Xenes can be destroyed by interlayer interaction with the supporting substrate [24, 25].

Dirac fermions were also observed in surface states of three-dimensional topological insulators[26-29], which, however, exist only in samples with nearly-perfect crystalline order[30], thus limiting considerably their application capabilities.

A suitable alternative is represented by the quest of other materials exhibiting Dirac fermions in the bulk. Especially, Dirac semimetals show linear dispersion along the three directions in the momentum space. Although several materials have been recently demonstrated to belong to the class of Dirac semimetals [31-34], most of them are unsuitable for applications. Specifically, Na_3Bi [35] is unstable even in ultrahigh vacuum (UHV); $PtTe_2$ [36] and $PdTe_2$ [37] are particularly expensive, owing to the presence of Pt and Pd atoms; $AgBi_2O_3$ [38] is challenging for crystal growth, especially in its stoichiometric form. Conversely, Cd_3As_2 provides robust 3D Dirac fermions coming from

bulk states [31, 39], which are also located in the nearness of the Fermi level, in contrast with the cases of $PtTe_2$ [36] and $PdTe_2$ [37]. In addition, 3D Dirac points in Cd_3As_2 are protected by crystal symmetry and robust against perturbations [40]. Cadmium arsenide is a novel topological semimetal hosting three-dimensional Dirac fermions with potential applications [41-45] exploiting ultrahigh mobility of charge carriers ($\sim 10^7$ cm^2 V^{-1} s^{-1} at T=5 K [46]) and linear magnetoresistance with giant values (1670% at 14 T and T=2 K [47]). Recently, Cd_3As_2 has been used to implement ultrafast photodetectors [48, 49] showing broadband response from mid-infrared up to visible, with responsivity as high as ~6 mA/W with a response time of ~7 ps[49]. Moreover, Cd_3As_2 represents a candidate for saturable absorbers for pulsed lasers in the infrared range [50] and terahertz harmonic generation [51, 52]. Furthermore, Nb-Cd_3As_2-Nb Josephson junctions have been recently proposed [53] for topological quantum devices.

Definitely, devices based on Cd_3As_2 should work in ambient conditions, i.e. in humid environment. Hence, the interaction of Cd_3As_2 surface with water is crucial in order to assess the stability in ambient atmosphere and potential technology transfer of research on Cd_3As_2. As a matter of fact, many innovative materials show important drawbacks in humid conditions. As an example, perovskites [54] and black phosphorus [55] are prone to hydroxylation and oxidation in humid atmosphere, respectively. In Bi_2Se_3 topological insulator, water induces band bending, with a shift of Dirac point and the formation of quantum well states with a strong Rashba-type splitting [56]. Even nearly inert materials, such as graphene, suffer of water-induced hydrogenation of defect sites, due to water splitting [57].
Another crucial issue is related to eventual site-dependent reactivity, since surface preparation by cleavage of bulk crystals unavoidably creates various types of defects on the surface[58-60], including steps [61]. Especially, steps formed during cleavage fracture could represent the sites with highest reactivity [62-64].
The structure of Cd_3As_2 is unusually complex, being the unit cell of Cd_3As_2 composed by 160 atoms (96 Cd and 64 As) [65]. Therefore, the theoretical modelling of physicochemical phenomena at

the Cd_3As_2 surface represents a serious hurdle, considering the capabilities of state-of-the-art computational facilities. The natural cleavage plan is the (112), so that this surface represents the most appropriate model system. Early experimental scanning tunneling microscopy (STM) investigations concluded that the (112) surface of Cd_3As_2 is As- terminated [66]. Morerover, the effective use of Cd_3As_2 in technology is delayed by the notable difficulty in achieving samples with superior crystalline quality. However, the recent improvement of the single-crystal growth procedure proposed by our group [67] enables experimental investigations aimed at understanding chemical reactivity and ambient stability. Recently, we have demonstrated that the (112) surface reconstructs [65] (Figure 1b), with surface Cd atoms sinking down into the As-layer.

Herein, we provide insight on water interaction with (i) pristine, (ii) defective and (iii) oxidized Cd_3As_2 surfaces by first-principles calculations, complemented by surface-science investigations on (112)-oriented Cd_3As_2 single-crystal foils grown by the self-selecting vapor growth (SSVG) method. We found that, while the pristine Cd_3As_2(112) is prone to surface oxidation, this surface is inert to water molecules. Surface Cd and As vacancy sites enable water adsorption without decomposition. Water decomposition is energetically feasible only at steps, with H and OH groups forming bonds with As and Cd atoms, separately. The decomposition barrier of water at steps is 0.84 eV, which is about twice higher than surface oxidation barrier. On the contrary, surface oxidation notably increases the reactivity towards water, also enabling water decomposition on the (112) surface of Cd_3As_2. Water splits on oxidized Cd_3As_2 surface with an energy barrier of only 0.29 eV and with a rate of 10^8 s^{-1} at a partial pressure of 1 bar.

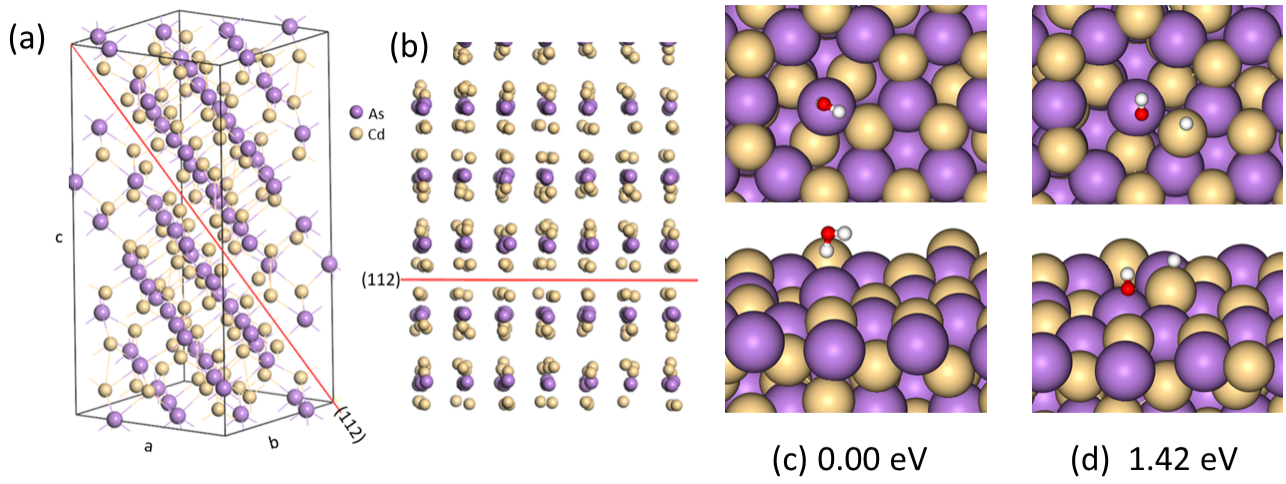

Figure 1. (a) The unit cell of Cd_3As_2, with 96 and Cd and As atoms, respectively. The (112) surface is indicated by the red plane, (b) the Cd-terminated (112) surface of Cd_3As_2, (c) top and side views of adsorption of water molecule on (112) surface of Cd_3As_2, (d) atomic bonding of H and hydroxyl with (112) surface after water decomposition. Purple, brown, white and red balls denote As, Cd, H and O atoms, respectively.

2 Results and Discussion

2.1 Theoretical model

Cd_3As_2 is a body-centered tetragonal with space group I41cd[68]. Its unit cell (Fig. 1a) can be viewed as a reconstructed (2 × 2 × 4) from a small sub-cell, where the As ions form a face-centered cubic, while the Cd ions fill 3/4 of the 8 tetragonal sites formed by the As ions. Our model provides values of lattice parameters a=b=12.632 Å and c=25.426 Å, in agreement with previous results [67] and our own XRD data (Supporting Information, SI, Figure S1).

To assess the stability of Cd_3As_2 surface in humid environments, we modelled water adsorption at room temperature. After structure relaxation, water molecules are stably adsorbed on the Cd_3As_2(112) surface (Fig. 1c), with an adsorption energy of 0.28 eV/H_2O. In the preferential adsorption geometry, one H atom points towards As sites of the surface, while OH lies parallel to the surface. The distance between H and As atom is ~2.6 Å, thus revealing a van der Waals interaction between H_2O and Cd_3As_2(112) surface. The decomposition of H_2O into H and OH fragments

chemisorbed at the surface is energetically unfavorable (Fig. 1d), since the total energy is 1.42 eV higher than water physisorption. This indicates that the defect-free Cd_3As_2(112) surface is unreactive towards H_2O and, consequently, it is stable in humid environments and water media. We further used Cd_3As_2(112) slabs with different thickness, the adsorption energies for both H_2O molecule and decomposed H and OH motifs are nearly the same (see Figure Sxxx), implying the model with 8.359 Å thickness is already enough.

To provide a more complete picture on water reactivity, it is crucial to assess the role of defects. Firstly, we considered water interaction with As (Fig. 2) and Cd (Fig. 3) vacancy sites. Two probable configurations for H_2O adsorption on As vacancy sites are identified (Fig. 2a-b). In both configurations, O-H bonds are parallel to the surface of Cd_3As_2, although a minimal difference (only 0.003 eV) concerning the orientation of the H_2O molecule exists.

Moreover, we examined water splitting at As vacancies for the two identified structures in Fig. 2a-b, resulting into H and OH bonded with Cd_3As_2. The decomposition pathway illustrated in Fig. 2c involves the formation of one H_2 molecule and an O atom embedded into the As vacancy. The total energy of this decomposition configuration is 0.85 eV higher than that of molecular physisorption (Fig. 2a). Accordingly, this decomposition pathway is energetically unfeasible. The total energy related to water splitting into OH and H fragments adsorbed at As vacancies is higher by 1.19 eV compared to molecular physisorption. Therefore, the presence of As vacancy sites at the Cd_3As_2 surface does not modify the chemical inertness of Cd_3As_2 to water.

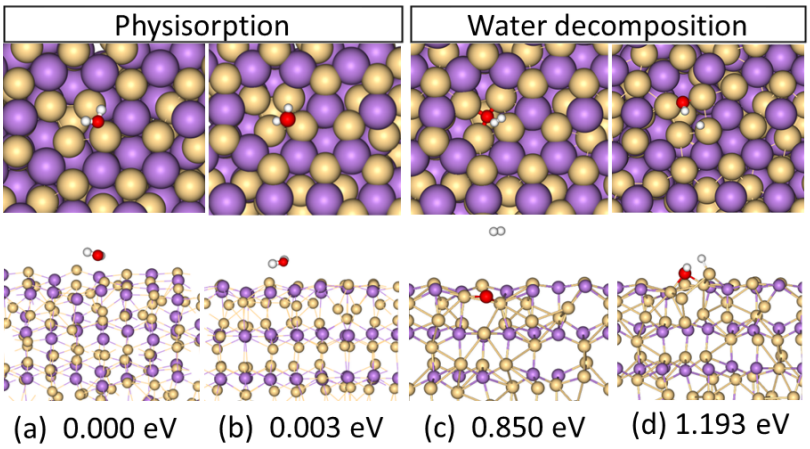

Figure 2. (a, b) Top and lateral views of H_2O adsorption configuration at As vacancy sites of the Cd_3As_2(112) surface; (c, d) The most probable bonding configuration for H, O, and OH adsorbed at the As vacancy site of (112) surface of Cd_3As_2 after water decomposition. Purple, brown, white and red balls denote As, Cd, H and O atoms, respectively.

We also consider the case of water adsorption at surface Cd-vacancy sites. The H atoms of H_2O point towards the surface of Cd_3As_2 for both physisorption configurations (Fig. 3a-b). The energy difference between the two physisorption configurations is only 0.007 eV, mainly originated by the orientation of the O-H bond. The adsorption energy of H and OH at Cd vacancy sites is 0.78 eV higher than that of molecular physisorption, implying the water does not decompose at surface Cd vacancies in Cd_3As_2(112). Therefore, we can conclude that the pristine and defective (112)-oriented Cd_3As_2 surface is inert to water even in the presence of As and Cd vacancy sites.

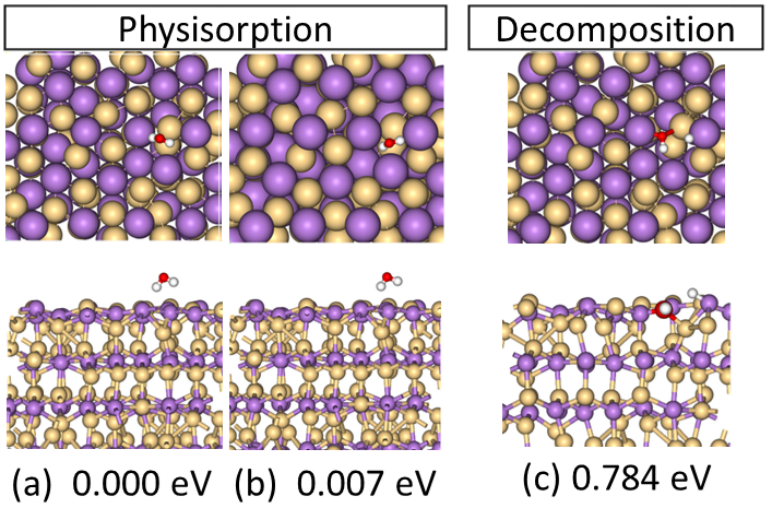

Figure 3. (a) Top and (b) side views of the adsorption configuration for H_2O adsorption at one Cd vacancy site of Cd_3As_2(112) surface. Panel (c) shows the most probable bonding configuration of H and OH fragments adsorbed at one Cd vacancy site of the (112) surface of Cd_3As_2 after water decomposition. Purple, brown, white and red balls denote As, Cd, H and O atoms, respectively.

Steps are other common defects at surfaces, which represent active sites in catalytic processes at surfaces [69]. To assess the impact of steps on water reactivity, we evaluated water adsorption at the stepped (112) surface of Cd_3As_2. Figure 4a shows the adsorption geometry for water physisorbed near the step. Interestingly, water splitting into H and OH fragments bonded to an atomic step is more energetically favorable than physisorption (total energy -0.2 eV/H_2O). Hydroxyl groups arising from water splitting are bonded with two Cd atoms, while hydrogen fragments form a chemical bond with As atom (Fig. 4b). Therefore, Cd_3As_2 steps and terraces differently interact with water and, specifically, stepped Cd_3As_2 surfaces can split water.

The transition path and the decomposition barrier from physisorbed H_2O to H+OH bonded to step were evaluated by using climbing-image Nudged Elastic Band (cNEB) [70, 71] method embedded in the VASP code. The decomposition barrier ΔE for water results to be 0.84 eV, while the average water decomposition rate is:

$$\left(\frac{k_B T}{h}\right) \times exp\left(-\Delta E / k_B T\right) \qquad (1)$$

where T is the temperature, k_B and h are the Boltzmann and Planck constants, respectively. At room temperature (T=300 K), the decomposition rate of water molecules is about 0.1 s^{-1} at partial pressure of water gas of 1 bar. Correspondingly, one can estimate the threshold water dose for decomposition at steps, which results to be $7.5 \cdot 10^9$ L (1 L=10^{-6} Torr·s), with a saturation H and OH coverage increasing with the step density in the sample. Therefore, the stability of Cd_3As_2 in water is proven, even in the presence of vacancies and steps.

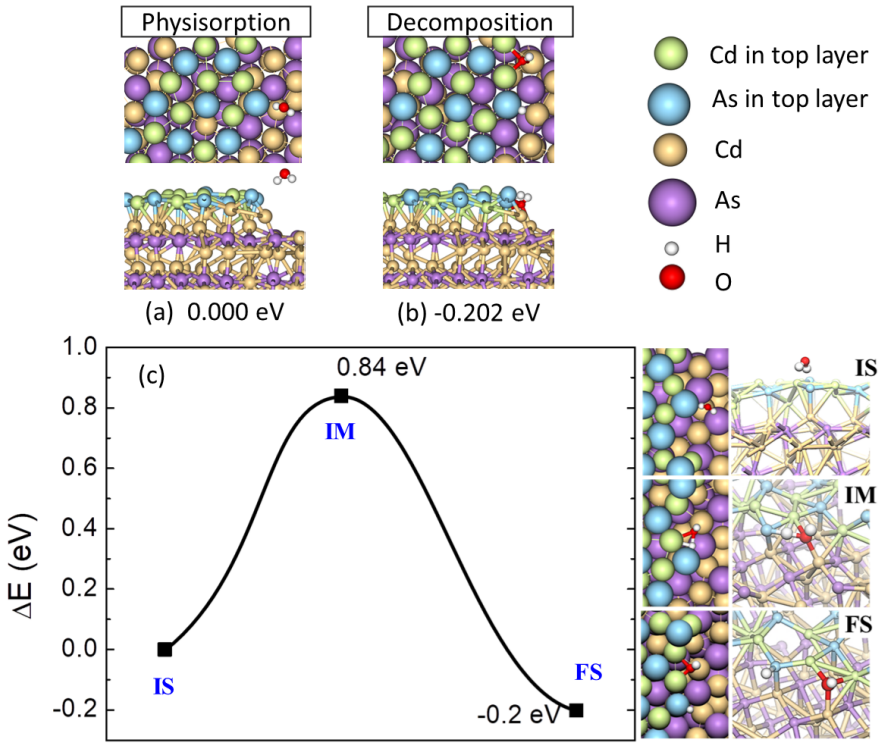

Figure 4. (a) Top and lateral views of the configuration of H_2O physisorption near the step of Cd_3As_2(112) surface; (b) the most probable bonding configuration of H and OH bonded at one atomic step of the (112) surface of Cd_3As_2 after H_2O decomposition; (c) the transition path and barrier from H_2O physisorption to decomposition in H and OH fragments. Green, blue, brown, purple, white and red balls denote Cd in the outermost surface layer, As in the outermost surface layer, bulk Cd, bulk As, H and O atoms, respectively. IS, IM and FS represent initial state, intermediate state and final state, respectively.

Although the (112) surface is prone to oxidation in air, the bulk properties of Cd_3As_2, including those connected to Dirac-cone electrons, are not affected by surface oxidation, owing to its topological protection demonstrated in Refs. [72, 73]. Therefore, it is important to explore also water interaction with oxidized Cd_3As_2 surface. Remarkably, we find that oxidation dramatically changes the interaction between water and Cd_3As_2 surface. Especially, in the oxidized surface the total energy for water chemisorption is reduced by 0.74 eV compared to the configuration for physisorption (Figure 5a-b), with a further reduction to -1.15 eV for water splitting (Figure 5c). The energy barrier from chemisorption to atomic decomposition is only 0.29 eV, as obtained by DFT calculations (Figure 5d). Therefore, water chemisorption on oxidized Cd_3As_2 surface is energetically favorable, with further splitting with a rate of about 10^8 H_2O s^{-1} at room temperature at a partial pressure of 1 bar, which corresponds to a threshold water exposure of 7.5 L.

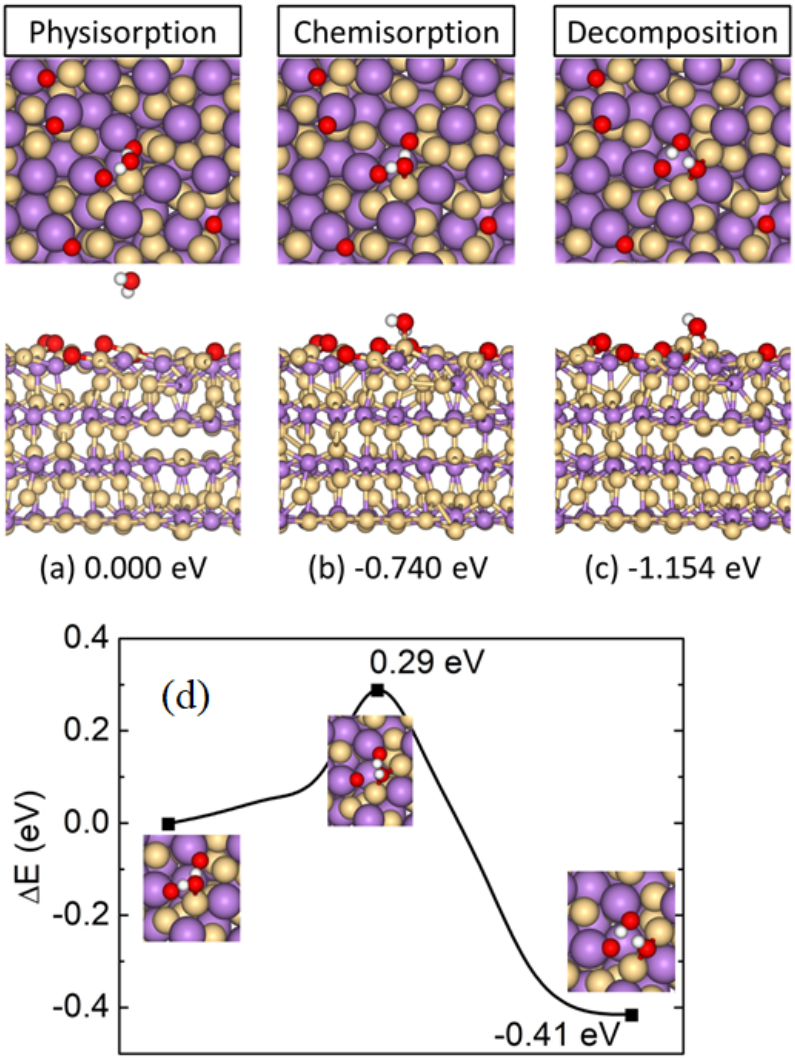

Figure 5. (a) Top and lateral views of the configuration of (a) physisorption and (b) molecular chemisorption of H_2O on the oxidized Cd_3As_2 (112) surface; (c) the configuration of O-H bonding after water decomposition on the oxidized Cd_3As_2; (d) the transition path and barrier from H_2O chemisorption to decomposition into OH motifs.

2.2 Validation by surface-science experiments

The analysis of core levels could provide important information in order to unveil surface chemical reactivity. However, conventional X-ray photoelectron spectroscopy (XPS) has insufficient surface sensitivity. Therefore, we used low-energy photons by means of synchrotron radiation-based XPS in order to drastically reduce the probing depth of impinging photons, thus gaining surface sensitivity. Figure 6 reports As-3d (panel a) and Cd-4d (panel b) core levels for the as-cleaved Cd_3As_2 and

their modification after exposure to different doses of H_2O from 23 L up to $1 \cdot 10^6$ L. Consistently with previous works[65, 67], the binding energy (BE) of As-$3d_{5/2}$ and Cd-$4d_{5/2}$ was found to be 40.5 eV (Fig. 6a) and 10.9 eV (Fig. 6b), respectively, with a spin-orbit separation between J=5/2 and J=3/2 components of 0.7 eV. No change in As-3d spectra was detected for H_2O exposure at room temperature up to doses as high as $2 \cdot 10^4$ L. Nevertheless, a new weak doublet, whose area is just 5.2% of the total spectral region of As-3d, appeared at 41.1 eV (J=5/2) after exposure to $2 \cdot 10^4$ L of H_2O. The intensity of this component slightly increased up to only 6% for higher H_2O doses ($1 \cdot 10^6$ L). Its BE matches with the formation of a small amount of elemental As(0) [65, 74, 75]. The emergence of this weak As doublet could be ascribed to segregation of amorphous As, similarly to recent findings for GaAs oxidation [76]. A possible interaction of As atoms with H fragments arising from water splitting at the atomic steps (which can be originated during the cleavage in UHV) seems unlikely because no evidence of the concomitant formation of Cd-OH bonds was observed. In fact, the line-shape of the Cd-4d doublet (Fig. 6b) remained unchanged upon H_2O exposure up to $1 \cdot 10^6$ L, while a negligible variation of the overall peak intensity (only 5% of the total area) was detected, consistently with the presence of small amounts of physisorbed contaminants on the surface. The absence of detectable changes in both Cd-4d (Fig. 6b) and Cd-3d (Figure S3a, SI) doublets suggests the inertness of Cd sites towards H_2O, excluding water splitting and the resulting interaction of Cd atoms with OH groups, at the H_2O doses used for the XPS experiment, which are well below the threshold of $7.5 \cdot 10^9$ L predicted by first-principle calculations for stepped surfaces.

It is worth noting that the amount of oxygen-related species was very low even for a dose of water of $1 \cdot 10^6$ L, as evident from the inspection of O-1s spectra in SI, Fig. S4a, in which two weak peaks were recorded at BEs of 531.6 (C-O/C-OH due to residual contamination) and 533.1 (physisorbed H_2O) eV, respectively.

To provide information about the valence electrons, responsible for the chemical bonds and the electronic structure near the Fermi level (mainly As-4p and Cd-5s states), we also probed the valence band (SI, Fig. S2b). The very tiny changes in the valence band line-shape even after exposure

to H_2O doses as high as 10^6 L, further confirm the inertness of defect-free Cd_3As_2 surface towards H_2O, as predicted by DFT calculations.

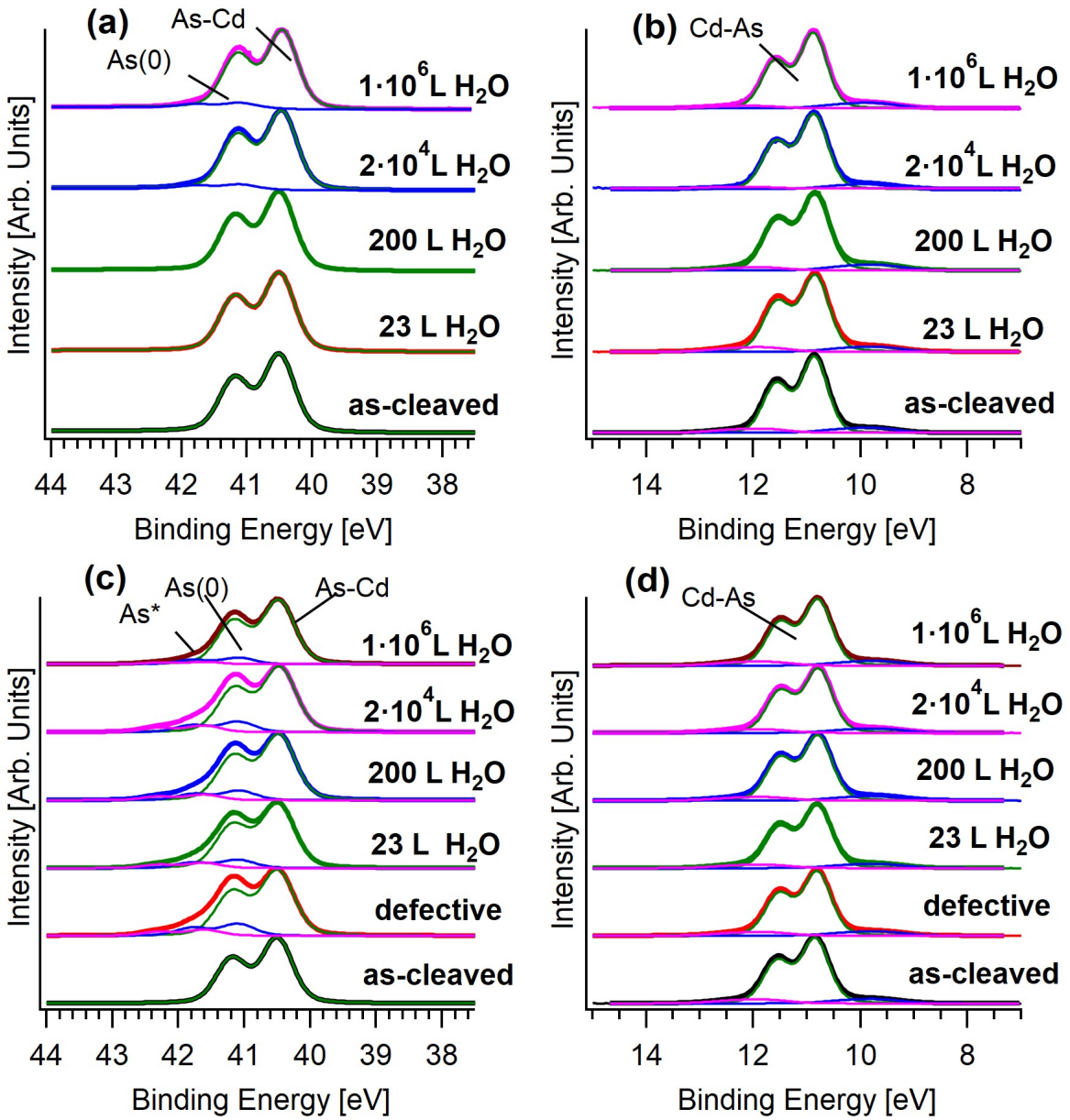

Figure 6. As-3d and Cd-4d core-levels for as-cleaved Cd_3As_2 (top) and defective Cd_3As_2 surfaces (bottom) exposed to 23 L, 200 L, $2.3 \cdot 10^4$ L and $1.1 \cdot 10^6$ L of H_2O. The incident photon energy used to measure As-3d, Cd-4d is 596 eV. Note that the weak feature around 10 eV in panels (b) and (d) is ascribed to the As-4s core level [77].

With the aim to probe H_2O interaction with defective Cd_3As_2 surface, the as-cleaved sample was modified by sputtering with Ar ions (flux ≈ 10^{19} ions/cm^2). After sputtering two new doublets appear in As-3d spectra (Figure 6c) at BEs of 41.1 eV and 41.5 eV (J=5/2), which can be attributed to metallic As(0) and to species with higher oxidation state (As*) arising from the creation of As defects, respectively [65, 74, 78]. The formation of steps and terraces on the surface is likely to occur with the sputtering, although the increase of the As concentration observed in XPS suggests the formation of As agglomerates. Conversely, no changes were detected on Cd-4d (Figure 6d) and Cd-3d (SI, Figure S3b) core levels, confirming the absence of eventually implanted Cd defects. Similarly to the case of as-cleaved Cd_3As_2, no changes were observed on Cd-4d and Cd-3d spectra upon water exposure (up to a dose of 10^6 L), confirming the inertness of Cd sites towards H_2O. Correspondingly, As-3d core-level spectra showed a significant reduction of the overall intensity of As* and As(0) components (from 21% to 5 % of the total spectrum area) after dosing $2 \cdot 10^4$ L of water, which suggests a preferential physisorption of H_2O on defects and As sites at the surface. For the highest vapour dose of $1 \cdot 10^6$ L, a coverage of about 0.2±0.1 ML of water was estimated from the attenuation of the As-3d core levels. The analysis of the O-1s core level (SI, Fig. S4c) indicates that the component related to adsorbed H_2O appears only above $2 \cdot 10^4$ L, in agreement with the preferential physisorption of small amounts of water on As sites.

Moreover, we investigated the interaction of water with oxidized Cd_3As_2 surface. Figure 7 reports the evolution of As-3d (panel a-b) and Cd-4d (panel c) core levels of oxidized Cd_3As_2 exposed to humid environments. Upon O_2 exposure, As-3d and Cd-4d doublets were down-shifted by 0.23 eV, due to O_2 intercalation in the subsurface region. The appearance of new As-3d components at higher BEs is associated with the oxidation of Cd_3As_2 surface (see Figure 7b). We attribute the new doublets with J=5/2 at 40.8 eV, 42.1 eV and 43.5 eV in As-3d core levels to (i) the segregation of As(0) species, (ii) the formation of hybrid As-O-Cd bonds [65] and (iii) As_2O_3 [78], respectively. It is worth noting that the corresponding BEs were slightly lower than in previous reports [76, 79, 80], due to

O_2 intercalation. Correspondingly, Cd-4d core levels displayed a new doublet with J=5/2 at BE~11 eV ascribed to hybrid Cd-O-As bonds, which is visible also in Cd-3d spectra at BE~405.3 eV (Figure S4, SI). After exposure to 10^5 of H_2O, a new component emerged in As-3d spectrum at a BE of 43.8 eV, while the overall intensity of As_2O_3 and As-O-Cd decreased from 25% to 14% of the total spectrum area, as a consequence of their conversion into species at higher oxidation state or, alternatively, of the formation of hydroxylated species (mainly As-OH bonds) [81]. The intensity of the new As-3d doublet at high BE further increased after dosing 10^6 L of H_2O (from 7% to 13% of the total spectrum area), together with the suppression of the As_2O_3 component (from 8% to 2% of the total spectrum area). The analysis of O-1s spectra (Fig. 7d) suggests that the formation of As-OH species is more likely than the formation of other oxides, such as As_2O_5. This is corroborated by the fact that, after exposing the oxidized Cd_3As_2 surface to 10^6 L of H_2O, the intensity of As-O component at BE=530.3 eV decreased from 33.5% to 15.5%, while the intensity of the components at 532.7 and 533.8 eV, ascribable to hydroxyls [82, 83] and to a multilayer of adsorbed H_2O, respectively, increased from 24% to 44%. The higher spectral weight of adsorbed H_2O molecules in O-1s spectra is ascribed to naturally superior affinity of hydroxylated species towards water.

XPS results are consistent with the proposed theoretical model. Specifically, experimental results indicate that oxidized Cd_3As_2 surface (pink curve in Fig. 7) is more reactive than the as-cleaved one (red curve reported in Fig. 7 for comparison) towards H_2O at the same dose (i.e., 10^6 L). Moreover, the observation of components in O-1s spectra related to hydroxyl bonds after H_2O exposure indicates the occurrence of water splitting on oxidized Cd_3As_2.

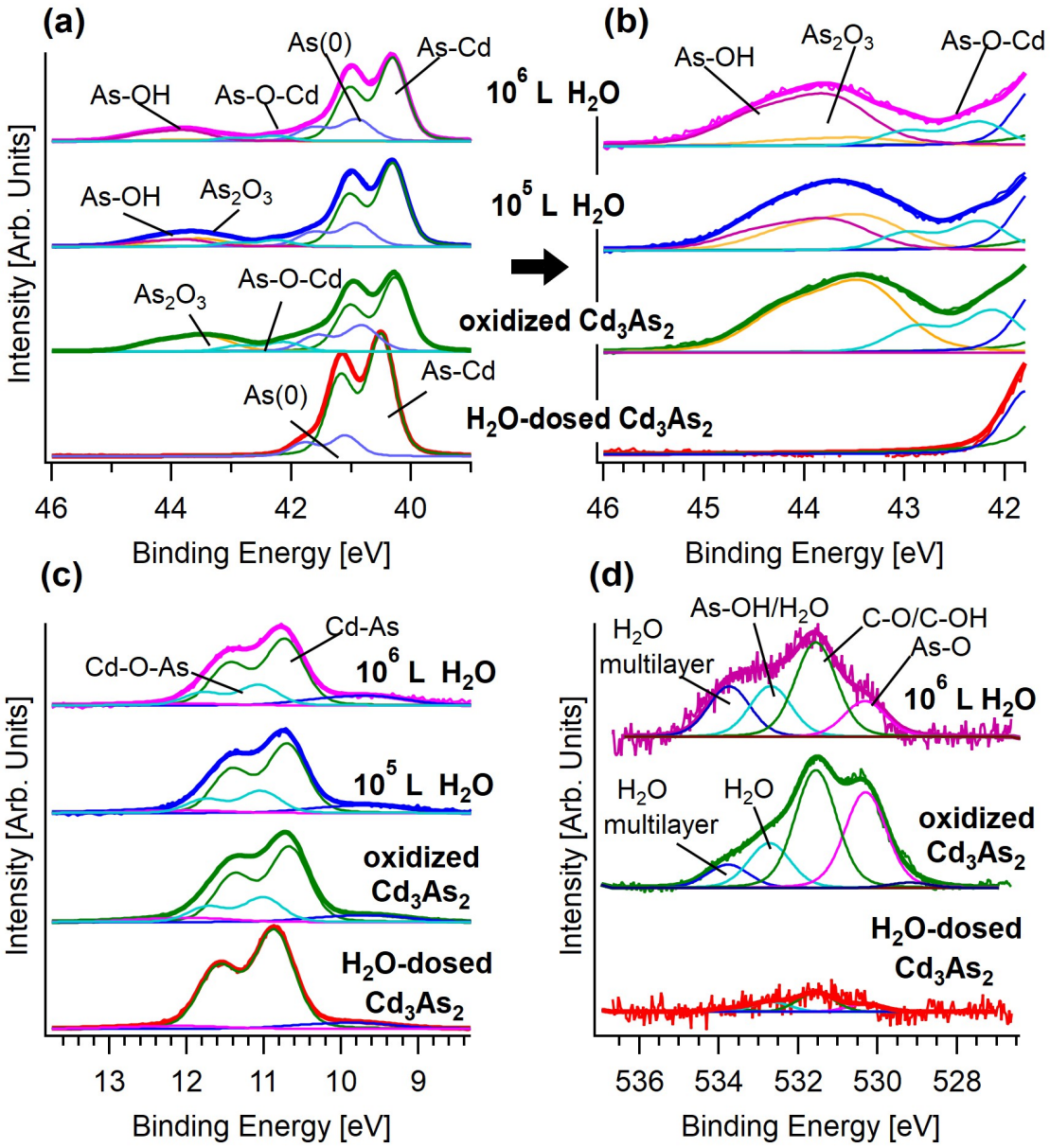

Figure 7. (a, b) As-3d, (c), Cd-4d and (d) O1-s core-levels of the oxidized Cd_3As_2 surface obtained by exposing the as-cleaved sample to $5 \cdot 10^4$ L of O_2 (green curve) and of the same surface after exposure to 10^5 (blue curve) and 10^6 L (pink curve) of H_2O at room temperature. Panel (b) is a magnification of panel (a) in the spectral region of arsenic oxides. The spectrum of pristine Cd_3As_2 surface exposed to 10^6 L of H_2O (red curve) is reported as a reference. The incident photon energy for As-3d and Cd-4d core levels (panels a-c) was set to 190 eV to gain high surface sensitivity, while O-1s (panel d) was measured with a photon energy of 610 eV.

2.2 Surface chemical bonds probed by vibrational spectroscopy

Important information on water adsorption on oxidized Cd_3As_2 surfaces can be gained by the analysis of the vibrational spectrum, which directly probes surface chemical bonds.

We calculated the infrared (IR) response spectrum of O-H vibrations before and after decomposition on the oxidized Cd_3As_2 (112) surface. For physisorption, two IR-active O-H bands are observed at 3713 (p1 peak in Fig. 8) and 3826 cm^{-1} (p2 peak in Fig. 8). These modes represent O-H stretching vibrations in nearly free-standing H_2O molecule. In contrast, for the case of chemisorption, the O-H region shows vibrational modes at lower energies, i.e., 3110 (p3 peak in Fig. 8) and 3576 cm^{-1} (p4 peak in Fig. 8). In all cases, the formation of a chemical bond between O in water with surface atoms limits the vibration of O-H bond. For a clearer visualization of atomic displacements associated to these vibrations, see the related movies (S-p1, S-p2, S-p3, S-p4 in the SI). Explicitly, for p1 and p2, two O-H bonds of water vibrate oppositely together, while only one O-H bond stretching can be clearly observed in p3 and p4.

Calculations were validated by vibrational experiments. Among vibrational spectroscopies, high-resolution electron energy loss spectroscopy (HREELS) has the highest surface sensitivity, practically coinciding with the outermost surface layer [84]. The O-H band measured by HREELS for H_2O-dosed oxidized Cd_3As_2 was dominated by a broad mode at 3686 cm^{-1} (457 meV). Another feature at 3371 cm^{-1} (418 meV) is present, which corresponds to the formation of a hydrogen bonding network involving H_2O agglomeration from molecules adsorbed at vacancy sites. Correspondingly, its intensity increases with the amount of water dose. The comparison with theoretical vibrational spectra in Fig. 8 indicates the occurrence of chemisorption of H_2O on the oxidized Cd_3As_2 surface.

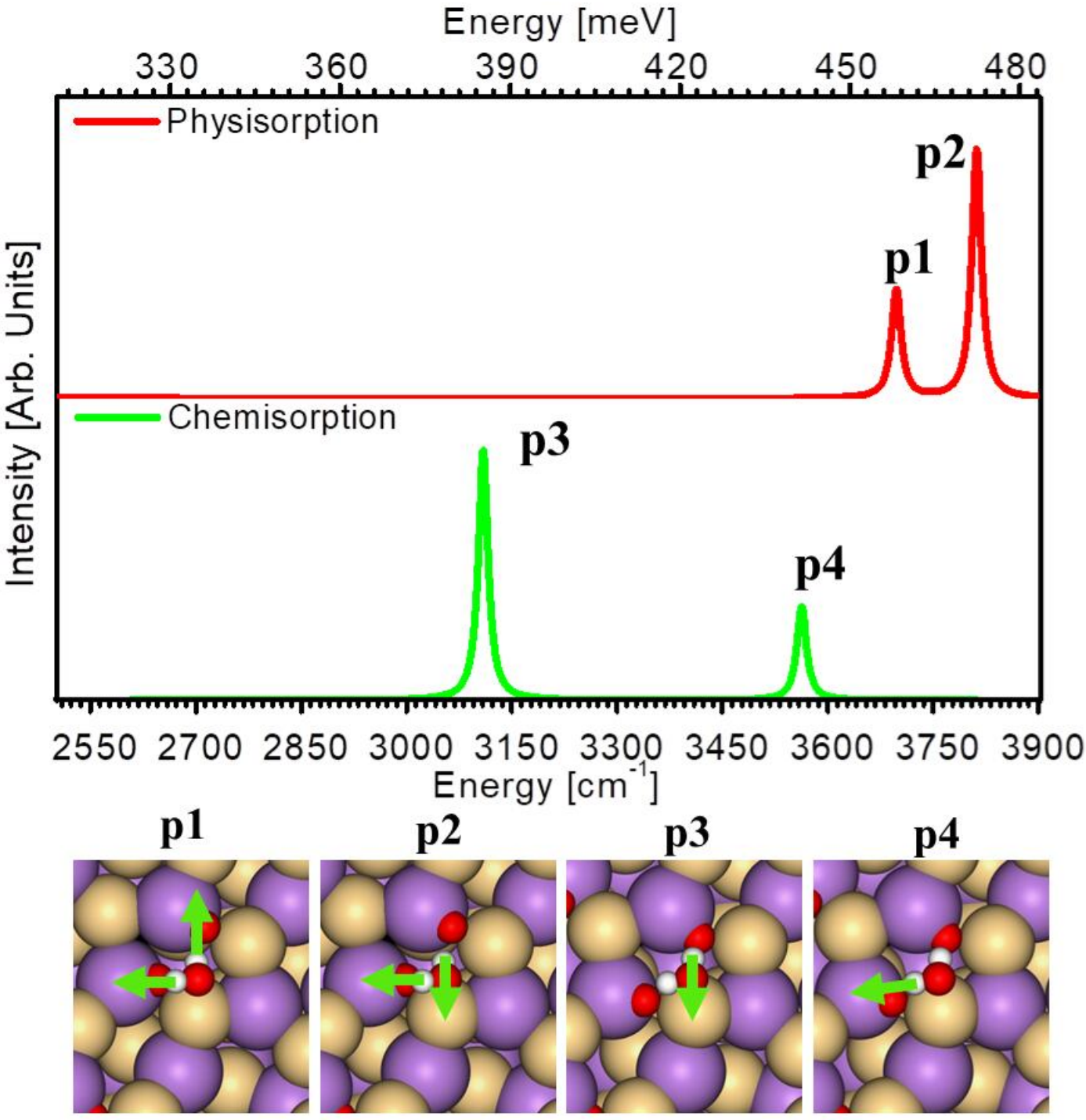

Figure 8. (Top panel) Infrared vibrational spectrum of physisorbed (red curve) and chemisorbed (green curve) water on oxidized Cd_3As_2 (112) surface. The corresponding infrared related vibrational modes are depicted as p1 (see S-P1 movie), p2 (see S-P2 movie), p3 (see S-P3 movie) and p4 (see S-P4 movie), respectively.

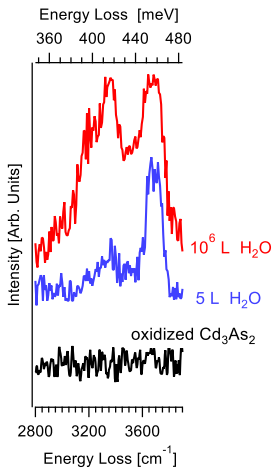

Figure 9: HREELS spectra for the oxidized Cd_3As_2 surface modified by the exposure of 5 and 10^6 L of H_2O at room temperature. The primary electron beam energy is 4 eV.

3 Conclusions

The stability of Cd_3As_2 in humid environment was assessed by studying surface reactivity towards water in pristine, defective, stepped and oxidized surfaces. We find that the pristine Cd_3As_2 surface is stable in humid environments: water does not form chemical bonds on Cd_3As_2 and, consequently, water splitting is ineffective even in the presence of point defects like Cd and As vacancies. As a matter of fact, only water physisorption is energetically favourable at both Cd- and As-vacancy sites.

On the other hand, in stepped Cd_3As_2 surfaces, the adsorption of water fragments is more energetically favourable than molecular physisorption by -0.2 eV. However, the water decomposition barrier remains as high as 0.84 eV and the decomposition rate of water molecules is about 0.1 s^{-1} at partial pressure of water gas of 1 bar. Considering the limited number of steps even in highly defective samples, water splitting results to be energetically unfeasible even on stepped surfaces. A drastic change in water reactivity occurs for the case of the oxidized Cd_3As_2(112) surface, for which the water decomposition barrier is dramatically reduced to only 0.29 eV, with stable chemisorption of water fragment.

Our study reveals the crucial role of surface oxidation in the stability of the Cd_3As_2 surface in humid environments (including ambient atmosphere). Consequently, encapsulation is necessary in order to protect the Cd_3As_2 surface from both oxidation and hydroxylation. Correspondingly, the presence of oxide patches at Cd_3As_2 surfaces could dramatically influence their wettability.

Methods

Theoretical methods

All first-principles calculations were performed by using the Vienna *ab-initio* simulation package (VASP) [85, 86] . Generalized gradient approximation (GGA) with the Perdew–Burke–Ernzerhof (PBE) functional [87] was used to describe the exchange-correlation interaction. Core electrons were descripted by the projector-augmented wave (PAW) technology [88]. A plane-wave basis kinetic energy cutoff of 400 eV and a convergence criterion of 10^{-5} eV were used in the calculations. All configurations were fully relaxed until the force is lower than 0.02 eV/Å. We adopted only Γ sampling

for structural relaxation. After fully relaxation, the vibration frequencies at Γ point were calculated, and related vibration modes were shown in supporting movies.

Single-crystal growth

Growth of single crystals was carried out following procedures presented in Ref. [67]. An effective growth provides flat (112)-oriented single-crystalline foils, as shown in the inset of Fig. S1 in the SI, as indicated by X-ray diffraction data reported in Fig. S1 in the SI.

The Cd_3As_2 samples were cleaved in UHV by post-method with natural cleavage plane coinciding with the (112) orientation. The analysis of the survey XPS spectrum indicated the absence of contaminants (SI, Fig. S2). Low-energy electron diffraction (LEED) image of as-cleaved surfaces exhibits first-order diffraction spots with hexagonal symmetry against a low background (SI, Fig. S6), thus confirming the effective cleavage along the (112) orientation.

Surface oxidation was achieved by a dosage of $4.5 \cdot 10^4$ L of O_2 at room temperature.

Surface-science spectroscopic methods

Spectroscopic experiments were carried out in two separate UHV apparatuses with a base pressure in the 10^{-10} mbar range and at room temperature in both cases. Water was dosed by leak valves. Vibrational experiments have been performed by using an electron energy loss spectrometer (Delta 0.5, SPECS) with an energy resolution of 3-4 meV. XPS experiments were carried out at the CNR beamline BACH at the Elettra synchrotron-Trieste, by using a Scienta R3000 hemispherical analyzer with an energy resolution of 0.1 eV. XPS spectra were acquired in normal incidence. A Shirley background was subtracted from raw XPS spectra and the resulting peaks were fitted with by Voigt line-shapes.

ACKNOWLEDGMENTS

This work was financially supported by the National Natural Science Foundation of China (No. 12074053, 91961204, 11664028), XinLiaoYingCai Project of Liaoning province, China (XLYC1907163) and the Start-Up grant of DUT [DUT20RC(5)026]. YZ and JG acknowledge the computing resource from the Supercomputing Center of Dalian University of Technology and ShangHai Supercomputing Center. AP thanks Elettra Synchrotron for access to the BACH beam-line. SN and FB acknowledge the EUROFEL project (RoadMap Esfri).

REFERENCES

1. C. In and H. Choi, *Adv. Opt. Mater.*, 2019, 1801334.
2. H. A. Hafez, S. Kovalev, J. C. Deinert, Z. Mics, B. Green, N. Awari, M. Chen, S. Germanskiy, U. Lehnert, J. Teichert, Z. Wang, K. J. Tielrooij, Z. Liu, Z. Chen, A. Narita, K. Müllen, M. Bonn, M. Gensch and D. Turchinovich, *Nature*, 2018, **561**, 507-511.
3. C. Kumar, M. Kuiri, J. Jung, T. Das and A. Das, *Nano Lett.*, 2016, **16**, 1042–1049.
4. L. Meng, J. Wu, Y. Li and J. Zhong, *J. Mater. Chem. C*, 2019, **7**, 12151-12159.
5. S. G. Xu, Z. J. Chen, Y. J. Zhao, X. Zhang, H. Xu and X. B. Yang, *J. Mater. Chem. C*, 2020, **8**, 2798-2805.
6. K. Bairagi, S. Catalano, F. Calavalle, E. Zuccatti, R. Llopis, F. Casanova and L. E. Hueso, *J. Mater. Chem. C*, 2020, **8**, 8120-8124.
7. Z. Y. Chen and R. Qin, *J. Mater. Chem. C*, 2020, **8**, 12085-12091.
8. F. Chianese, F. Chiarella, M. Barra, A. Candini, M. Affronte and A. Cassinese, *J. Mater. Chem. C*, 2020, **8**, 8145-8154.
9. S. R. Lee, P. A. Sharma, A. L. Lima-Sharma, W. Pan and T. M. Nenoff, *Chem. Mater.*, 2019, **31**, 26-51.
10. G. S. Thakur, P. Vir, S. N. Guin, C. Shekhar, R. Weihrich, Y. Sun, N. Kumar and C. Felser, *Chem. Mater.*, 2020, **32**, 1612-1617.
11. R. Roldán, J. N. Fuchs and M. O. Goerbig, *Phys. Rev. B*, 2009, **80**, 085408.
12. M. Richter, A. Carmele, S. Butscher, N. Bucking, F. Milde, P. Kratzer, M. Scheffler and A. Knorr, *J. Appl. Phys.*, 2009, **105**, 122409.
13. M. Yi and Z. Shen, *J. Mater. Chem. A*, 2015, **3**, 11700-11715.
14. D. Marchenko, A. Varykhalov, M. Scholz, G. Bihlmayer, E. Rashba, A. Rybkin, A. Shikin and O. Rader, *Nat. Commun.*, 2012, **3**, 1-6.
15. I. I. Klimovskikh, S. S. Tsirkin, A. G. Rybkin, A. A. Rybkina, M. V. Filianina, E. V. Zhizhin, E. V. Chulkov and A. M. Shikin, *Phys. Rev. B*, 2014, **90**, 235431.
16. A. Grüneis and D. V. Vyalikh, *Phys. Rev. B*, 2008, **77**, 193401.
17. A. Al Taleb and D. Farías, *Journal of Physics: Condensed Matter*, 2016, **28**, 103005.
18. R. Qin and Z. Y. Chen, *Nanoscale*, 2018, **10**, 22593-22600.
19. P. Gori, I. Kupchak, F. Bechstedt, D. Grassano and O. Pulci, *Phys. Rev. B*, 2019, **100**.
20. J. Zhuang, C. Liu, Z. Zhou, G. Casillas, H. Feng, X. Xu, J. Wang, W. Hao, X. Wang and S. X. Dou, *Adv. Sci.*, 2018, **5**, 1800207.
21. S. Gupta, A. Kutana and B. I. Yakobson, *J. Phys. Chem. Lett.*, 2018, **9**, 2757-2762.
22. B. Feng, O. Sugino, R.-Y. Liu, J. Zhang, R. Yukawa, M. Kawamura, T. Iimori, H. Kim, Y. Hasegawa, H. Li, L. Chen, K. Wu, H. Kumigashira, F. Komori, T.-C. Chiang, S. Meng and I. Matsuda, *Phys. Rev. Lett.*, 2017, **118**, 096401.

23. A. Molle, G. Faraone, A. Lamperti, D. Chiappe, E. Cinquanta, C. Martella, E. Bonera, E. Scalise and C. Grazianetti, *Faraday Discuss.*, 2020, doi:10.1039/C1039FD00121B.
24. Y. Wang, J. Li, J. Xiong, Y. Pan, M. Ye, Y. Guo, H. Zhang, R. Quhe and J. Lu, *Phys. Chem. Chem. Phys.*, 2016, **18**, 19451-19456.
25. R. Quhe, Y. Yuan, J. Zheng, Y. Wang, Z. Ni, J. Shi, D. Yu, J. Yang and J. Lu, *Sci. Rep.*, 2014, **4**, 5476.
26. H. Pirie, Y. Liu, A. Soumyanarayanan, P. Chen, Y. He, M. Yee, P. Rosa, J. Thompson, D.-J. Kim and Z. Fisk, *Nat. Phys.*, 2019, 1-5.
27. I. Vobornik, U. Manju, J. Fujii, F. Borgatti, P. Torelli, D. Krizmancic, Y. S. Hor, R. J. Cava and G. Panaccione, *Nano Lett.*, 2011, **11**, 4079-4082.
28. M. Z. Hasan and C. L. Kane, *Rev. Mod. Phys.*, 2010, **82**, 3045-3067.
29. A. Zeugner, F. Nietschke, A. U. B. Wolter, S. Gaß, R. C. Vidal, T. R. F. Peixoto, D. Pohl, C. Damm, A. Lubk, R. Hentrich, S. K. Moser, C. Fornari, C. H. Min, S. Schatz, K. Kißner, M. Ünzelmann, M. Kaiser, F. Scaravaggi, B. Rellinghaus, K. Nielsch, C. Hess, B. Büchner, F. Reinert, H. Bentmann, O. Oeckler, T. Doert, M. Ruck and A. Isaeva, *Chem. Mater.*, 2019, **31**, 2795-2806.
30. V. V. Atuchin, V. A. Golyashov, K. A. Kokh, I. V. Korolkov, A. S. Kozhukhov, V. N. Kruchinin, S. V. Makarenko, L. D. Pokrovsky, I. P. Prosvirin, K. N. Romanyuk and O. E. Tereshchenko, *Cryst. Growth Des.*, 2011, **11**, 5507-5514.
31. I. Crassee, R. Sankar, W.-L. Lee, A. Akrap and M. Orlita, *Phys. Rev. Mater.*, 2018, **2**, 120302.
32. N. Armitage, E. Mele and A. Vishwanath, *Rev. Mod. Phys.*, 2018, **90**, 015001.
33. Q. D. Gibson, L. M. Schoop, L. Muechler, L. S. Xie, M. Hirschberger, N. P. Ong, R. Car and R. J. Cava, *Phys. Rev. B*, 2015, **91**, 205128.
34. C. Xu, B. Li, W. Jiao, W. Zhou, B. Qian, R. Sankar, N. D. Zhigadlo, Y. Qi, D. Qian, F.-C. Chou and X. Xu, *Chem. Mater.*, 2018, **30**, 4823-4830.
35. Z. K. Liu, B. Zhou, Y. Zhang, Z. J. Wang, H. M. Weng, D. Prabhakaran, S.-K. Mo, Z. X. Shen, Z. Fang, X. Dai, Z. Hussain and Y. L. Chen, *Science*, 2014, **343**, 864-867.
36. M. Yan, H. Huang, K. Zhang, E. Wang, W. Yao, K. Deng, G. Wan, H. Zhang, M. Arita and H. Yang, *Nat. Commun.*, 2017, **8**, 257.
37. H.-J. Noh, J. Jeong, E.-J. Cho, K. Kim, B. Min and B.-G. Park, *Phys. Rev. Lett.*, 2017, **119**, 016401.
38. B. Singh, B. Ghosh, C. Su, H. Lin, A. Agarwal and A. Bansil, *Phys. Rev. Lett.*, 2018, **121**, 226401.
39. M. Neupane, S.-Y. Xu, R. Sankar, N. Alidoust, G. Bian, C. Liu, I. Belopolski, T.-R. Chang, H.-T. Jeng, H. Lin, A. Bansil, F. Chou and M. Z. Hasan, *Nat. Commun.*, 2014, **5**, 3786.
40. H. Yi, Z. Wang, C. Chen, Y. Shi, Y. Feng, A. Liang, Z. Xie, S. He, J. He, Y. Peng, X. Liu, Y. Liu, L. Zhao, G. Liu, X. Dong, J. Zhang, M. Nakatake, M. Arita, K. Shimada, H. Namatame, M. Taniguchi, Z. Xu, C. Chen, X. Dai, Z. Fang and X. J. Zhou, *Sci. Rep.*, 2014, **4**, 6106.
41. C. Zhang, Y. Zhang, X. Yuan, S. Lu, J. Zhang, A. Narayan, Y. Liu, H. Zhang, Z. Ni, R. Liu, E. S. Choi, A. Suslov, S. Sanvito, L. Pi, H. Z. Lu, A. C. Potter and F. Xiu, *Nature*, 2019, **565**, 331-336.
42. Y. F. Wu, L. Zhang, C. Z. Li, Z. S. Zhang, S. Liu, Z. M. Liao and D. Yu, *Adv. Mater.*, 2018, **30**, 1707547.
43. S. Wang, B. C. Lin, W. Z. Zheng, D. Yu and Z. M. Liao, *Phys. Rev. Lett.*, 2018, **120**, 257701.
44. K. Park, M. Jung, D. Kim, J. R. Bayogan, J. H. Lee, S. J. An, J. Seo, J. Seo, J.-P. Ahn and J. Park, *Nano Lett.*, 2020, **20**, 4939-4946.
45. A. Chanana, N. Lotfizadeh, H. O. Condori Quispe, P. Gopalan, J. R. Winger, S. Blair, A. Nahata, V. V. Deshpande, M. A. Scarpulla and B. Sensale-Rodriguez, *ACS Nano*, 2019, **13**, 4091-4100.
46. T. Liang, Q. Gibson, M. N. Ali, M. Liu, R. J. Cava and N. P. Ong, *Nat. Mater.*, 2015, **14**, 280–284.
47. H. Li, H. He, H. Z. Lu, H. Zhang, H. Liu, R. Ma, Z. Fan, S. Q. Shen and J. Wang, *Nat. Commun.*, 2016, **7**, 10301.
48. M. Yang, J. Wang, J. Han, J. Ling, C. Ji, X. Kong, X. Liu, Z. Huang, J. Gou and Z. Liu, *ACS Photonics*, 2018, **5**, 3438-3445.
49. Q. Wang, C. Z. Li, S. Ge, J. G. Li, W. Lu, J. Lai, X. Liu, J. Ma, D. P. Yu, Z. M. Liao and D. Sun, *Nano Lett.*, 2017, **17**, 834-841.
50. Y. Meng, C. Zhu, Y. Li, X. Yuan, F. Xiu, Y. Shi, Y. Xu and F. Wang, *Opt. Lett.*, 2018, **43**, 1503-1506.
51. B. Cheng, N. Kanda, T. N. Ikeda, T. Matsuda, P. Xia, T. Schumann, S. Stemmer, J. Itatani, N. P. Armitage and R. Matsunaga, *Phys. Rev. Lett.*, 2020, **124**, 117402.

52. S. Kovalev, R. M. A. Dantas, S. Germanskiy, J. C. Deinert, B. Green, I. Ilyakov, N. Awari, M. Chen, M. Bawatna, J. Ling, F. Xiu, P. H. M. van Loosdrecht, P. Surówka, T. Oka and Z. Wang, *Nat. Commun.*, 2020, **11**, 2451.
53. C. Z. Li, A. Q. Wang, C. Li, W. Z. Zheng, A. Brinkman, D. P. Yu and Z. M. Liao, *Nat. Commun.*, 2020, **11**, 1150.
54. K. A. Stoerzinger, W. T. Hong, G. Azimi, L. Giordano, Y.-L. Lee, E. J. Crumlin, M. D. Biegalski, H. Bluhm, K. K. Varanasi and Y. Shao-Horn, *J. Phys. Chem. C*, 2015, **119**, 18504-18512.
55. W. Luo, D. Y. Zemlyanov, C. A. Milligan, Y. Du, L. Yang, Y. Wu and P. D. Ye, *Nanotechnology*, 2016, **27**, 434002.
56. H. M. Benia, C. Lin, K. Kern and C. R. Ast, *Phys. Rev. Lett.*, 2011, **107**, 177602.
57. G. He, Q. Wang, H. K. Yu, D. Farías, Y. Liu and A. Politano, *Nano Res.*, 2019, **12**, 3101-3108.
58. J. Dickinson, L. Jensen, R. Webb, M. Dawes and S. Langford, *J. Appl. Phys.*, 1993, **74**, 3758-3767.
59. A. Ismail, A. B. Brahim, J. Palau and L. Lassabatere, *Surf. Sci.*, 1985, **162**, 195-201.
60. F. Proix and F. Houzay, *J. Phys. C*, 1980, **13**, 1845.
61. B. Stegemann, C. Ritter, B. Kaiser and K. Rademann, *Phys. Rev. B*, 2004, **69**, 155432.
62. C. R. Thomas, M. K. Vallon, M. G. Frith, H. Sezen, S. K. Kushwaha, R. J. Cava, J. Schwartz and S. L. Bernasek, *Chem. Mater.*, 2016, **28**, 35-39.
63. G. Füchsel, K. Cao, S. l. Er, E. W. Smeets, A. W. Kleyn, L. B. Juurlink and G.-J. Kroes, *The journal of physical chemistry letters*, 2018, **9**, 170-175.
64. S. Ferrer, J. Rojo, M. Salmeron and G. Somorjai, *Philos. Mag. A*, 1982, **45**, 261-269.
65. J. Gao, A. Cupolillo, S. Nappini, F. Bondino, R. Edla, V. Fabio, R. Sankar, Y. W. Zhang, G. Chiarello and A. Politano, *Adv. Funct. Mater.*, 2019, **29**, 1900965.
66. S. Jeon, B. B. Zhou, A. Gyenis, B. E. Feldman, I. Kimchi, A. C. Potter, Q. D. Gibson, R. J. Cava, A. Vishwanath and A. Yazdani, *Nat. Mater.*, 2014, **13**, 851-856.
67. R. Sankar, M. Neupane, S. Y. Xu, C. J. Butler, I. Zeljkovic, I. Panneer Muthuselvam, F. T. Huang, S. T. Guo, S. K. Karna, M. W. Chu, W. L. Lee, M. T. Lin, R. Jayavel, V. Madhavan, M. Z. Hasan and F. C. Chou, *Sci. Rep.*, 2015, **5**, 12966.
68. G. Steigmann and J. Goodyear, *Acta Crystallogr. B*, 1968, **24**, 1062-1067.
69. B. L. Hendriksen, M. D. Ackermann, R. Van Rijn, D. Stoltz, I. Popa, O. Balmes, A. Resta, D. Wermeille, R. Felici and S. Ferrer, *Nature Chem.*, 2010, **2**, 730.
70. G. Henkelman and H. Jónsson, *J. Chem. Phys.*, 2000, **113**, 9978-9985.
71. G. Henkelman, B. P. Uberuaga and H. Jónsson, *J. Chem. Phys.*, 2000, **113**, 9901-9904.
72. Z. K. Liu, J. Jiang, B. Zhou, Z. J. Wang, Y. Zhang, H. M. Weng, D. Prabhakaran, S. K. Mo, H. Peng, P. Dudin, T. Kim, M. Hoesch, Z. Fang, X. Dai, Z. X. Shen, D. L. Feng, Z. Hussain and Y. L. Chen, *Nat. Mater.*, 2014, **13**, 677-681.
73. P. J. W. Moll, N. L. Nair, T. Helm, A. C. Potter, I. Kimchi, A. Vishwanath and J. G. Analytis, *Nature*, 2016, **535**, 266-270.
74. I. V. Sedova, M. V. Lebedev, G. V. Klimko, S. V. Sorokin, V. A. Solov'ev, G. Cherkashinin, S. Nappini, E. Magnano, M. N. Drozdov, P. S. Kop'ev and S. V. Ivanov, *Appl. Surf. Sci.*, 2018, **448**, 455-464.
75. M.-S. Park, M. Razaei, K. Barnhart, C. L. Tan and H. Mohseni, *J. Appl. Phys.*, 2017, **121**, 233105.
76. D. Shahrjerdi, D. I. Garcia-Gutierrez, T. Akyol, S. R. Bank, E. Tutuc, J. C. Lee and S. K. Banerjee, *Appl. Phys. Lett.*, 2007, **91**, 193503.
77. F. Bondino, E. Magnano, C. Booth, F. Offi, G. Panaccione, M. Malvestuto, G. Paolicelli, L. Simonelli, F. Parmigiani and M. McGuire, *Phys. Rev. B*, 2010, **82**, 014529.
78. C. Wang, S. Wang, G. Doornbos, G. Astromskas, K. Bhuwalka, R. Contreras-Guerrero, M. Edirisooriya, J. Rojas-Ramirez, G. Vellianitis and R. Oxland, *Appl. Phys. Lett.*, 2013, **103**, 143510.
79. T. Kumar, M. Kumar, G. Gupta, R. K. Pandey, S. Verma and D. Kanjilal, *Nanoscale Res. Lett.*, 2012, **7**, 1-8.
80. S. Colonna, A. Terrasi, S. Scalese, F. Iacona, V. Raineri, F. La Via and S. Mobilio, *Surf. Sci.*, 2003, **532-535**, 746-753.
81. H. W. Nesbitt and M. Reinke, *Am. Mineral.*, 1999, **84**, 639-649.
82. S. R. Sanivarapu, J. B. Lawrence and G. Sreedhar, *ACS Omega*, 2018, **3**, 6267-6278.

83. A. Kolmakov, D. A. Dikin, L. J. Cote, J. Huang, M. K. Abyaneh, M. Amati, L. Gregoratti, S. Günther and M. Kiskinova, *Nat. Nanotechnol.*, 2011, **6**, 651-657.
84. H. Ibach, *Surf. Sci.*, 1994, **299**, 116-128.
85. G. Kresse and J. Furthmüller, *Comp. Mater. Sci.*, 1996, **6**, 15-50.
86. G. Kresse and J. Furthmüller, *Phys. Rev. B*, 1996, **54**, 11169-11186.
87. J. P. Perdew, K. Burke and M. Ernzerhof, *Phys. Rev. Lett.*, 1996, **77**, 3865-3868.
88. P. E. Blöchl, *Phys. Rev. B*, 1994, **50**, 17953-17979.